Spatially resolved x-ray spectroscopy investigation of femtosecond laser irradiated Ar clusters

G. C. Junkel-Vives,[1] J. Abdallah, Jr.,[1] T. Auguste,[2] P. D'Oliveira,[2] S. Hulin,[2] P. Monot,[2] S. Dobosz,[2] A. Ya. Faenov,[3] A. I. Magunov,[3] T. A. Pikuz,[3] I. Yu. Skobelev,[3] A. S. Boldarev,[4] and V. A. Gasilov[4]

[1]*Theoretical Division, T-4, Los Alamos National Laboratory, P.O. Box 1663, Los Alamos, New Mexico 87545*

[2]*Commissariat à l'Energie Atomique, Centre D'Etudes de Saclay, DSM/DRECAM, Bâtiment 522, 91191 Gif-sur-Yvette, France*

[3]*Multicharged Ions Spectra Data Center of VNIIFTRI, Mendeleevo, 141570 Moscow Region, Russia*

[4]*Institute of Mathematical Modeling, Russian Academy of Science, Moscow 125047, Russia*

(Received 4 June 2001; revised manuscript received 17 October 2001; published 27 February 2002)

High temperature plasmas have been created by irradiating Ar clusters with high intensity 60-fs laser pulses. Detailed spectroscopic analysis of spatially resolved, high resolution x-ray data near the He_α line of Ar is consistent with a two-temperature collisional-radiative model incorporating the effects of highly energetic electrons. The results of the spectral analysis are compared with a theoretical hydrodynamic model of cluster production, as well as interferometric data. The plasma parameters are notably uniform over one Rayleigh length (600 μm).

DOI: 10.1103/PhysRevE.65.036410 PACS number(s): 52.50.Jm, 36.40.Gk, 52.70.La

I. INTRODUCTION

The interaction of high-power, ultrashort laser pulses with matter, particularly atomic gas clusters, has been a subject of active investigation in recent years. Such investigations have advanced fundamental research and understanding of the behavior of matter under extreme conditions [1–12]. Laser interactions with clusters have been studied extensively as sources of intense x-rays as well as for the generation of highly energetic particles for practical applications in fusion research, medical and biological imaging, and microscale lithography [1,2,13].

The actual study of cluster formation has been limited, particularly with respect to the spatial structure of cluster parameters. Previous work relied upon the empirical theory developed by Hagena [14–16] to describe cluster formation. In addition, Rayleigh scattering [1] was used in some experiments to evaluate the parameters of the clusters generated. A summary of the studies of clustering can be found in Ref. [17]. These approaches allow for the evaluation of conditions of cluster formation, as well as determination of the average size of a cluster and the density of clusters; however, they do not consider in detail the processes taking place in the gas jet. In particular, the obtained parameters describe an average over the whole gas jet, while there is no information about their spatial and temporal resolution. Meanwhile, some experimental results can be explained only by using the detailed information about the spatial distribution of clusters, which can only be obtained from the modeling of the processes taking place in a jet.

In cases where the spatial characteristics of laser produced plasmas are of interest, relevant experimental work can be found mostly in the study of laser self-focusing and plasma channel formation [18–21]. Although the goal of the current investigation is primarily the analysis of hard x-ray production and the modeling of cluster formation within the jet, similar phenomena were observed and useful comparisons can be made with self-focusing experiments. Channel formation allows laser guiding for distances longer than the Rayleigh length without significant energy loss or diffraction. The Rayleigh length is defined as $z_r = \omega_0 r_L^2/2c$, where r_L is the laser spot size radius. Plasma channels are characterized by a low density region along the path of laser propagation, where the strong laser field has expelled the electrons, surrounded by a region of high electron density. This configuration enhances the index of refraction along the edges of the path and focuses the laser energy down the channel. If the laser power exceeds critical power P_{crit} this process overcomes the effect of diffraction and can allow the pulse to travel many times the Rayleigh length. On the other hand, if P_{crit} is not exceeded, the laser pulse experiences diffraction and the plasma is vulnerable to instabilities [21–26]. In addition, experiments involving channeling are sensitive to density gradients in the target gas [26–28]. Optimum laser absorption leading to the rapid onset of channeling occurs when the laser focus is coincident with the large gradient at the edge of the gas jet [21,28]. These previous studies point to a need to know the spatial distribution the target material.

Self-channeling experiments conducted on gas-jet [18,21], solid [29] and cluster targets [19,20,30,31], have demonstrated many similarities among them. In the present paper, we will investigate the spatial distribution of plasma radiation from cluster targets and contrast our results with previous self-focusing experiments. The laser intensity employed in the current experiment is less than that used for typical self-focusing experiments. Such experiments usually employ intensities $> \sim 10^{18}$ W/cm^2. Also, self-channeling experiments have used laser pulses that range from 600 ps to 250 fs. The current experiment uses a much shorter main pulse 60 fs, although the prepulse is on the order of 1 ps.

One unique cluster experiment [20] employed a moderate intensity prepulse $\sim 10^{13}$ W/cm^2 to predissociate Ar clusters along the path of laser propagation. Since clusters absorb the laser energy much more efficiently than isolated atoms, only the wings of the main pulse were absorbed by clusters still existing in the annular region surrounding the dissociated Ar atoms, creating the necessary low electron density channel surrounded by a high density plasma. The current experiment is quite different since it uses a lower intensity prepulse. We wish to complete dissociation of the clusters by the prepulse,

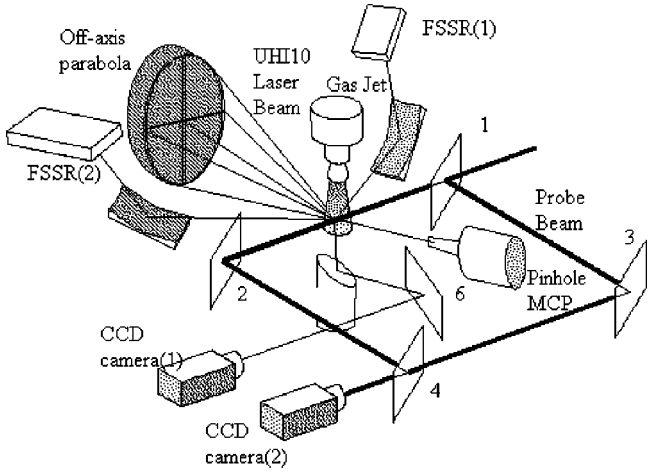

FIG. 1. A schematic of the experimental setup is shown. The 80-mm-diameter laser beam is focused with an $f/6.25$ off-axis parabolic mirror. Two focusing spectrometers with spatial resolution (FSSR) are shown as well as a pinhole camera and two charge-coupled device (CCD) cameras to obtain an interferogram.

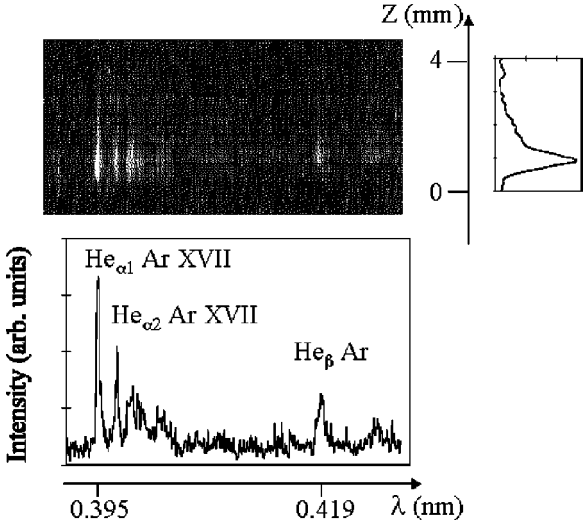

FIG. 2. Spatially resolved Ar *K*-shell spectrum is shown. The data were obtained over 4 mm in the longitudinal direction. The He$_\alpha$ as well as the He$_\beta$ can be clearly seen with their B-, Be-, and Li-like satellites. The He$_\beta$ is obtained from the fifth-order mica reflection, while the He$_\alpha$ is obtained from the fourth-order reflection.

which would inhibit the production of x-rays. In addition, the main pulse used in the current experiment has a much higher intensity than that described in Ref. [20]. Finally, the current experiment used significantly larger clusters than many self-channeling experiments [19,30,31], which may have also allowed the clusters to survive the prepulse [32].

In the present paper, a detailed simulation of the two-phase gas dynamic processes in the nozzle, which forms the jet, is presented and the spatial distribution of cluster parameters is obtained. This model was applied to the conditions of a laser-cluster experiment performed on the UHI10 laser installation at Saclay, France. This experiment will be described in Sec. II. In Sec. III, we describe the ''moments method'' approach, which was employed to model the cluster formation. This technique was developed mainly for the study of water-steam flows in nozzles and turbine cascades. The results of these calculations will be presented in Sec. IV. In Sec. V, the results of the cluster modeling will be compared to spatially resolved Ar *K*-shell spectra as well as interferometric data used to measure electron density, and pinhole imaging. The x-ray spectra was analyzed using a two-temperature kinetics model that incorporates the effects of hot electrons [33–35]. The results of the analysis will also be discussed in Sec. V. It will be shown that the hydrodynamic modeling agrees well with the observed cluster behavior. Also, the spectral and interferometric data are used to describe the behavior of the cluster plasma. The results will be summarized in Sec. VI.

II. EXPERIMENTAL SETUP

The experiments were performed on the UHI10 laser. The experimental setup is shown in Fig. 1. UHI10 is a two-beam 10-Hz Ti:sapphire laser system with wavelength $\lambda = 800$ nm. The main beam has a 10-TW peak power. The initial low-energy ultrashort pulse is produced by a modified commercial Ti:sapphire oscillator that is stretched up to 300 ps by an aberration-free Offner stretcher. After four amplification stages, the pulse is then recompressed down to 60 fs in a vacuum chamber that is directly connected to the experimental chamber. The contrast is measured to be about 10^{-5} at 1 ps on the main beam with a high dynamic cross correlator. The 80-mm-diameter laser beam is focused with an $f/6.25$ off-axis parabolic mirror. The $1/e^2$ focal spot radius is $r_L = 25\ \mu$m ($M^2 \sim 4$). The corresponding Rayleigh length and vacuum intensity are 600 μm and 7×10^{17} W/cm^{-2}, respectively. A small amount of the laser energy is peaked up between the third and fourth amplifiers for the second probing beam, which is then sent to a separate compressor. After recompression in air, this probing beam has a 4-mJ energy and is used for interferometric investigations.

A cluster target was formed by the adiabatic expansion in vacuum of an argon gas puff produced by a pulsed valve with a conical nozzle. An arrangement with a 1-mm input diameter, a 5-mm output diameter, and a 20-mm expansion length created the appropriate conditions to obtain a spectrum featuring the x-ray emission from multicharged ions. The laser was focused at the vacuum-gas interface, about 1.5 mm below the nozzle. The gas jet was characterized by laser interferometry. The density profile has a Gaussian shape with a 4-mm width (at $1/e$), and a peak atom density of 4.6×10^{18} cm^{-3} for a maximum gas backing pressure of 15 bars [34].

Figure 2 illustrates spatially resolved x-ray spectra of argon in the spectral range 3.35–4.2 Å, which were obtained by means of two focusing spectrometers with spatial resolution; see Ref. [36]. Spherically bent mica crystals with a radius of curvature, $R = 150$ mm, were used in these spectrometers. The crystal of the first spectrometer was placed 250 mm from the plasma. The middle Bragg angle was 71.7°. Wavelengths near the Ly$_\alpha$ of H-like Ar (3.72–3.82 Å) are in this spectral range, and correspond to the fifth order of the mica crystal reflection. The crystal of

the second spectrometer was placed 300 mm from the plasma. The middle Bragg angle was 56.6°. The fifth-order mica reflection allowed recording of the spectra near the n-$n'=3-1$, and $4-1$ transitions of He-like ArXVII. The spectral range between the He_α and K_α Ar line was observed in the fourth order of crystal reflection. It should be noted that our attempts to observe the Ly_α line of H-like ArXVIII were unsuccessful.

The theoretical spectral resolution of the fourth and fifth reflection orders of mica crystal approached $\lambda/\delta\lambda \sim 10\,000$ for the present geometry. The x-ray spectral images of Ar have been obtained with a demagnification of about 2.1–2.3 and a spatial resolution around 30-40 μm in the direction of propagation of the laser in the cluster jet, which is consistent with the focusing properties of the sperically bent crystal. The spectra were recorded on Kodak direct exposure film. The film cassette was protected by two layers of 1-μm polypropylene covered by 0.2 μm of Al, and by a 7-μm Be filter.

III. MATHEMATICAL MODEL OF TWO-PHASE GAS FLOW

There have been numerous studies of phase transitions in nozzle flows (for example, see [37,38] and the bibliography presented there). The water-steam system has received the most attention since the steam flows are widely used in power engineering. However, the approaches developed (theoretical consideration, mathematical models, etc.) are valid for an arbitrary gas flow with appropriate physical parameters. According to the conditions of our experiment, we consider a gas at low initial temperatures that does not contain ions.

The origination of the condensed phase (which shall be considered here to be the liquid phase) takes place due to density fluctuations in supersaturated gas, i.e., spontaneous condensation. The detailed presentation of the theory of spontaneous condensation can be found, for example, in Ref. [39]. Due to surface effects, a small liquid droplet can be in equilibrium or evaporate even in supersaturated gas (the surface tension provides an additional potential barrier for an atom entering the droplet). So, for particular parameters of the gas there is a critical value of droplet radius r_*. A droplet with radius r_* is in equilibrium with the gas, a smaller droplet evaporates and vanishes, and only the droplets with radii greater than r_* can grow in the gas with these parameters. We use the expression [38]

$$r_* = \frac{2\sigma}{\rho_l RT \ln(P/P_s)} \tag{1}$$

for the critical radius. Here σ is the surface tension coefficient, ρ_l is the density of liquid, $R = R_0/\mu$ is the gas constant, T and P are temperature and pressure, and $P_s = P_s(T)$ is the saturation pressure at temperature T.

To produce a condensation nucleus able to grow, the fluctuation resulting in the appearance of a droplet with radius $r > r_*$ must take place. The theory of fluctuations [40] gives the expression for the intensity of such fluctuations,

$$I = \frac{1}{\rho_l}\sqrt{\frac{2\sigma\mu}{\pi N_A}}\left(\frac{P}{kT}\right)^2 \exp\left(-\frac{4\pi\sigma r_*^2}{3kT}\right). \tag{2}$$

This value may be treated as the number of condensation nuclei appearing per unit time in unit volume of gas, where N_A is Avogadro's constant, μ is the mass per mole, and k is the Boltzmann constant.

To obtain the velocity of growth of the existing droplets, we use the expression [38]

$$\dot{r} = \frac{P}{\rho_l\sqrt{2\pi RT}}\left(1 - \sqrt{\frac{T}{T_s(P)}}\right), \tag{3}$$

where T and $T_s(P)$ are the temperatures of the gas and droplets, respectively. The temperature of a droplet is assumed to be independent of the droplet's radius. This assumption is valid if the growth of droplets takes place in the free atomic regime that is not limited by heat transfer. This supposition is necessary for further development of the model.

The current model of two-phase gas flow is based upon the following suppositions. The velocities of droplets are equal to the gas velocity. The droplet temperature is equal to the saturation temperature. The effects of breaking in and confluence of the droplets, viscosity, heat conductivity, and turbulence are negligibly small. There is no solid phase in the flow. Neither the possibility of freezing of droplets nor the solid nuclei origination is taken into account.

The model can be represented by the following system of differential equations:

$$\frac{\partial\rho}{\partial t} + \nabla\cdot(\rho\mathbf{v}) = 0, \tag{4}$$

$$\frac{\partial\rho\mathbf{v}}{\partial t} + \nabla\cdot(\rho\mathbf{v}\times\mathbf{v}) = -\nabla P, \tag{5}$$

$$\frac{\partial}{\partial t}\rho\left(e + \frac{\mathbf{v}^2}{2}\right) + \nabla\cdot\left[\rho\mathbf{v}\left(e + \frac{\mathbf{v}^2}{2}\right)\right] = -\nabla\cdot P\mathbf{v}, \tag{6}$$

$$\frac{\partial\rho\Omega_0}{\partial t} + \nabla\cdot(\rho\mathbf{v}\Omega_0) = I, \tag{7}$$

$$\frac{\partial\rho\Omega_1}{\partial t} + \nabla\cdot(\rho\mathbf{v}\Omega_1) = Ir_* + \dot{r}\rho\Omega_0, \tag{8}$$

$$\frac{\partial\rho\Omega_2}{\partial t} + \nabla\cdot(\rho\mathbf{v}\Omega_2) = Ir_*^2 + 2\dot{r}\rho\Omega_1, \tag{9}$$

$$\frac{\partial\rho\beta}{\partial t} + \nabla\cdot(\rho\mathbf{v}\beta) = -\frac{4}{3}\pi\rho_l I r_*^3 - 4\pi\rho\rho_l\dot{r}\Omega_2, \tag{10}$$

$$P = P(\rho,e,\beta) = \rho\left(\frac{e + (1-\beta)L_s}{\frac{\gamma}{\beta(\gamma-1)} - 1}\right), \tag{11}$$

$$T = \frac{P}{\beta Z\rho R}. \tag{12}$$

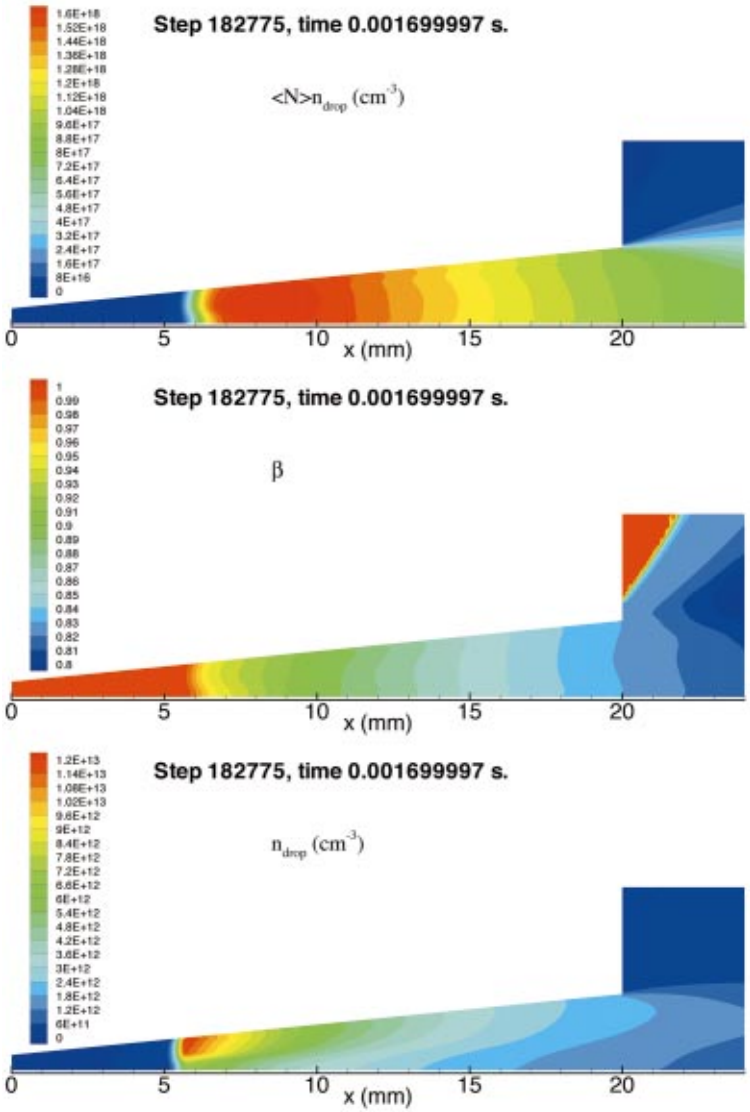

FIG. 3. (Color) Spatial distribution of $\langle N\rangle n_{\mathrm{drop}}$, the average density of atoms forming the liquid phase; β, the mass ratio of gas phase relative to the total mass; and n_{drop}, the number density of clusters in the nozzle. One can see that there is some spatial structure in the transverse direction of the cluster distribution, particularly for the cluster density n_{drop}, while the other parameters are quite uniform.

Here ρ is the density of the whole two-phase medium, $\mathbf{v}$ is its velocity, e is the internal energy per unit mass, and β is the mass ratio of the gas phase in the whole two-phase medium. The values Ω_i, $i=0,1,2$, are the moments of distribution function of the droplets. In Eqs. (11) and (12), L_s is the evaporation heat per unit mass, $\gamma=c_P/c_V$ is the specific heat ratio, Z is a compressibility coefficient.

IV. RESULTS OF CLUSTER PRODUCTION MODELING

To obtain the gas parameters within the jet, the system of equations (4)–(10) have been solved numerically using the relationships (1), (2), (3), (11), (12). The initial conditions correspond to a stationary gas with temperature T_0 and pressure $1\times10^{-6}P_0$, where P_0 and T_0 are the initial parameters of the gas in the vessel. The boundary condition at the walls of the nozzle was zero normal velocity, $(\mathbf{v}\cdot\mathbf{n})=0$, while at the inlet, boundary values were chosen so that the stagnation parameters were consistent with the values of P_0 and T_0, using the following expressions:

$$e+\frac{P}{\rho}+\frac{v^2}{2}=e_0+\frac{P_0}{\rho_0}, \tag{13}$$

$$S(P,\rho)=S(P_0,\rho_0). \tag{14}$$

Here, S is the entropy and the subscript 0 refers to the initial gas parameters in the vessel. Two-dimensional calculations were performed for the region inside the nozzle volume and some distance downstream from the nozzle's outlet. The nozzle modeled has a conical shape with an inlet diameter of 1 mm, an outlet diameter of 5 mm and a length 20 mm. Also, the initial parameters for argon are given by $P_0=15$ bars and $T_0=293$ K.

The results presented below correspond to some instant of time when the pattern of the flow becomes mostly stationary. The color isoline maps for the average density of atoms forming the liquid phase $\langle N\rangle n_{drop}$, the mass ratio of gas phase relative to the total mass β, and the number density of drops (or clusters) n_{drop} are presented in Fig. 3. Some spatial structure in the cluster distribution is evident, particularly in

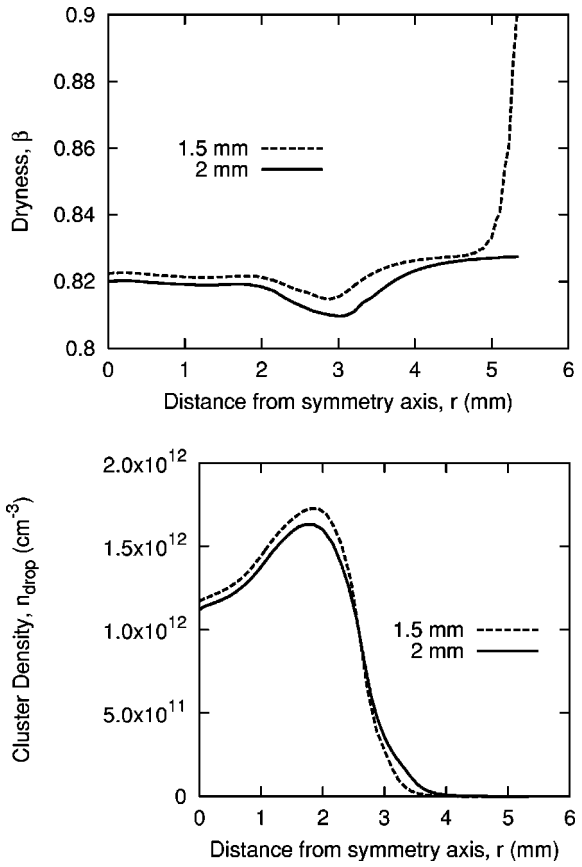

FIG. 4. Cross-section profiles of two parameters at 1.5 and 2 mm from nozzle's outlet are shown. The values presented are β, the mass ratio of gas phase to the total mass; n_{drop}, the density of clusters (droplets).

the distribution of number density of drops (or clusters) n_{drop}. On the other hand, the spatial structure for values of β and $\langle N\rangle n_{\mathrm{drop}}=(1-\beta)n_{\mathrm{atom}}$ are more homogeneous; they are nearly one dimensional. This seeming contradiction can be better understood if one considers that the cluster size, $\langle N\rangle$, and density, n_{drop}, may vary while $\langle N\rangle n_{drop}$ remains uniform.

The dependences of β, sometimes refered to as ''dryness,'' and cluster density n_{drop} as a function of distance from the jet's axis for the cross section positioned at distance 1.5 and 2 mm downstream from the nozzle's outlet are presented in Fig. 4. One can see that although there is some spatial structure of values presented, the changes of these values are relatively small, within a radius of approximately 2 mm. In addition, the average density of atoms, which is presented in Fig. 5, is practically constant across the jet, and its diminishing takes place only at distances $r\approx 2.5$ mm from the symmetry axis. Comparisons of experiment with the hydrodynamic calculations indicate that the model predicts the measured cluster parameters very well. The width of the density profile (4 mm diameter) agrees well with the measured profile and the peak atomic densities show a close correspondence, see Fig. 5. It should be briefly noted that the use of a Laval jet nozzle results in much less uniform densities and distribution of clusters. Further details concerning the modeling of Laval nozzles can be found in Ref. [41].

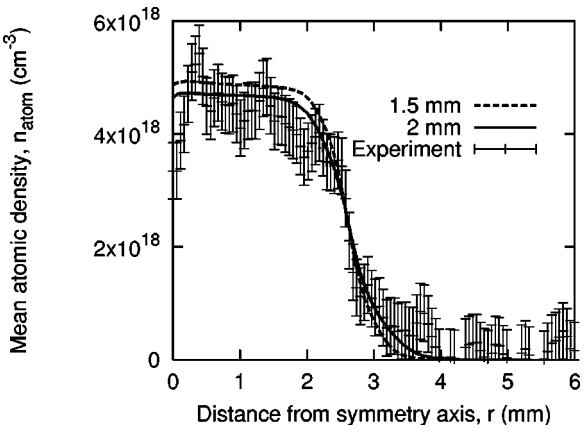

FIG. 5. Mean density of atoms n_{atom} as a function of the distance from jet's axis at 1.5 and 2 mm from the nozzle's outlet. The theoretical calculation is compared with experimental measurements, showing excellent agreement. We can see that the density begins to drop off dramatically at a diameter of 4 mm.

V. ANALYSIS OF SPECTRA AND DISCUSSION

Detailed spectroscopic analysis, incorporating the effects of hot electrons was conducted on spatially resolved Ar *K*-shell spectra obtained in the experiment described in Sec. II. In Fig. 2 is the spatially resolved *K*-shell spectra in which the He_{α}, its satellites, and the He_{β} are evident. Looking at the spectrally integrated profile inset to the right, the intensity strongly peaks at approximately 1000 μm and trails off so that the emission is indistinguishable from the background by $\sim$2500 μm.

Figure 6 shows the spatially integrated spectroscopic data in the region of the Ar He_{α}. The He_{α} and its satellites occur in the range from 3.93 to 4.05 Å, and are obtained from the fourth-order mica crystal reflection. Please note that the He_{γ} appears in the He_{α} spectrum from the fifth-order reflection off the crystal. This feature has been included in the model spectra, although its intensity relative to the He_{α} was arbi-

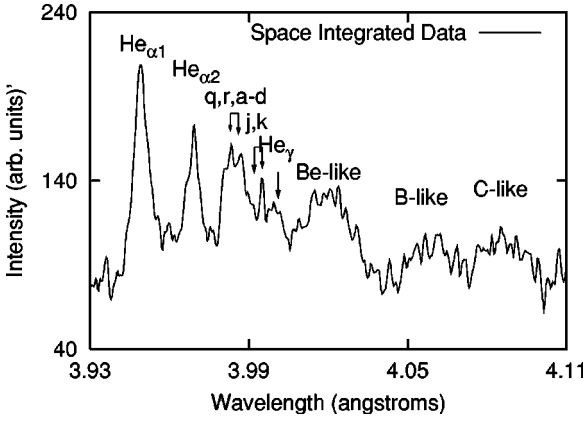

FIG. 6. Spatially integrated spectra of the Ar He_{α} and its satellites are shown. Specific features important to the analysis and diagnosis of the plasma are indicated.

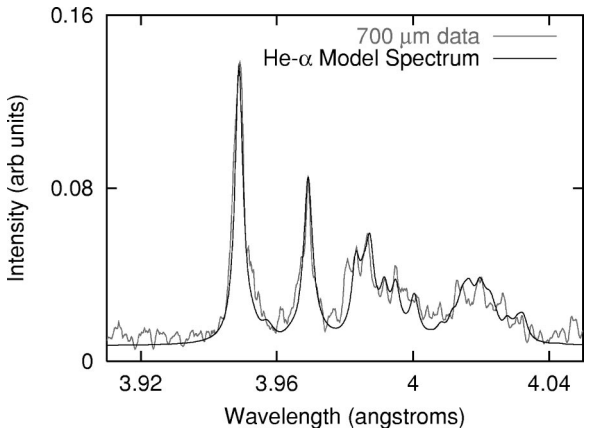

FIG. 7. For the spectral data shown above, the plasma is characterized by two sets of plasma parameters: $kT=230$ eV, $N_e=3\times10^{20}$ cm^{-3}, and hot electron fraction $f=7\times10^{-4}$; and $kT=130$ eV, $N_e=3\times10^{19}$ cm^{-3}, and $f=7\times10^{-8}$.

trary and is not used in the spectral analysis. The relative intensities of the He_α and its Li- and Be-like satellites provides detailed information about the electron density and temperature, as well as the hot electron fraction, since the presence of high-energy electrons enhance the populations of certain states via collisional excitation and ionization, such as those leading to the Li-like $q,r,a-d$ satellites of the Ar He_α indicated in Fig. 6.

In order to generate the theoretical spectra, the system of steady state radiative-collisional rate equations was solved for uniform plasma with different plasma parameters [42]. The rate coefficients for the electron collision processes were calculated using a model electron-energy distribution function, which includes a provision for hot electrons. The details of the calculations are described in detail in Refs. [33,34]. The spectral profiles were calculated using an instrumental resolution of $\lambda/\Delta\lambda=1400$.

The calculated model spectrum is shown with the spatially resolved experimental data for the spectral regions around the Ar He_α in Fig. 7. Note the excellent agreement between theory and experiment. The model spectra is a sum of spectra using two sets of plasma parameters: a high temperature, moderate density contribution, $kT=230$ eV, $N_e=3\times10^{20}$ cm^{-3}, with a hot electron fraction $f=7\times10^{-4}$; and a low temperature, low density contribution, $kT=130$ eV, $N_e=3\times10^{19}$ cm^{-3}, with hot electron fraction $f=7\times10^{-8}$. Table I lists the plasma parameters for the individual spatially resolved line outs. The spectra are dominated by the component with the higher electron density, sometimes as high as critical density, with the lower density component generating an extra contribution for Be-like satellites. However, the higher density component is only a small portion of the total plasma volume, of the order of 10^{-7} to 10^{-6}. The low density emission can come from the rarified plasma between clusters or from the clusters themselves after they expanded into their surroundings.

There is not a unique set of parameters that will fit the experimental spectrum. For example, the spectrum shown in Fig. 7 could be fit just as well with the temperatures $kT_{\text{high}}=250$ eV and $kT_{\text{low}}=160$ eV with greater hot electron fractions. In spite of this small ambiguity, the theoretical spectra generated from the current model is sufficiently sensitive to the plasma parameters that the temperatures are known within 10–15 % and the higher density is known within 20%. Finally, the lower density spectra are insensitive to the density up to $N_e=1\times10^{20}$ cm^{-3}, so the value used for the model spectra was chosen to be consistent with interferometry measurements.

TABLE I. Comparison of plasma parameters with longitudinal distance.

Distance (μm)	Bulk temperature (eV)	Electron density (cm^{-3})	Hot electron fraction
500	222	5×10^{20}	3×10^{-4}
	130	3×10^{19}	1.7×10^{-8}
600	222	5×10^{20}	3×10^{-4}
	130	3×10^{19}	1×10^{-8}
700	230	3×10^{20}	7×10^{-4}
	130	3×10^{19}	7×10^{-8}
900	205	5×10^{20}	3×10^{-4}
	130	5×10^{19}	1×10^{-7}
1100	>205	6.5×10^{20}	3×10^{-4}
	130	3×10^{19}	3×10^{-8}
1300	215	$>1.5\times10^{21}$	1.7×10^{-4}
	130	3×10^{19}	7×10^{-7}
1500	<215	$>1.5\times10^{21}$	1.7×10^{-4}
	130	3×10^{19}	$3\times10^{-}$
1700	265	$<2\times10^{20}$	$<3\times10^{-3}$
	130	3×10^{19}	1×10^{-7}
1900	265	$\ll2\times10^{20}$	3×10^{-3}
	130	3×10^{19}	$>1\times10^{-7}$

The spatially resolved spectroscopic data, along with interferometry data and pinhole imaging, provides detailed characterization of the cluster plasma. Although Ar *K*-shell emission was measured over a distance of 4 mm, as seen in Fig. 2, the quality of the first 500 μm of data was too poor to be analyzed. The results of the first 600 μm (500–1100 μm) of useful data indicate remarkably uniform plasma parameters and corresponds to the maximum Ar *K*-shell emission. Over the next 400 μm, the electron density increases to nearly critical density and falls rapidly below the values seen in the first region. In addition, the bulk electron temperature and hot electron fraction steadily increase over the same region; the total *K*-shell emission also falls over this region. The line emission beyond 1900 μm is difficult to distinguish from the background.

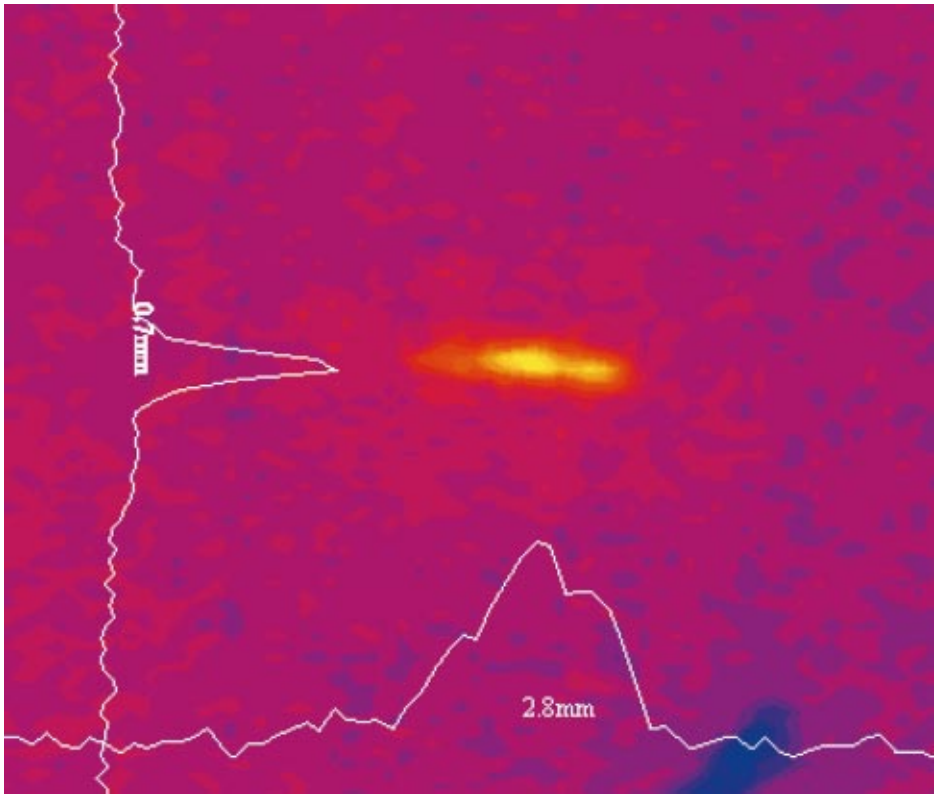

FIG. 8. (Color) Pinhole image of the cluster plasma.

The Ar x-ray spectral data is corroborated by an x-ray pinhole image and interferometry data shown in Figs. 8 and 9. In the pinhole image, the plasma appears to have an elongated shape approximately 2.8 mm long and 0.7 mm wide. The electron density profile obtained from interferometry measurements corresponds roughly with the size of the pinhole image, having a length of approximately 3.5 mm and a 0.8 mm width. This data agrees roughly with the hydrodynamic modeling. Also, the mean density of atoms shown in Fig. 5 is consistent with a maximum electron density of less than 8×10^{19} cm^{-3} if the argon were ionized to $+16$ (He-like). In comparison, interferometry data shows densities no higher than 3×10^{19} cm^{-3}. This is the maximum value of electron density that can be measured by optical interferometry using the current laser wavelength. The region of greatest electron density in the interferogram coincides with the high density region in the spectral data, including the sudden drop in density at 1.7 mm (3.4 mm on the interferogram). Also, unlike previous experiments where self-focusing was achieved [21,20], our interferogram does not show ridges along the path of the laser pulse characteristic of a plasma channel.

Besides finding agreement between the cluster modeling and experiment, we were able to gather other information about the laser-cluster interaction. Although the plasma was formed from a mixture of Ar gas and clusters, it was characterized by notably uniform temperatures and density for the first 600 μm, one Rayleigh length, in the direction of laser propagation. In addition, the maximum x-ray emission also occurred over this same region. Since the relevant length scale seems to be the Rayleigh length, diffraction must be important as the laser propagates through the plasma. This may explain the diminished x-ray emission along the laser propagation direction.

Beyond one Rayleigh length, however, we find a region of oscillating electron density, suggesting a Raman instability [22–25]. This sort of instability is seen in high-intensity laser-plasma experiments when the laser intensity is below the threshold for self-focusing and is competing with diffraction effects [23,21]. It is most pronounced when the power is below critical power P_{crit}, and channeling does not occur. Forward Raman scattering is also known to generate highly energetic electrons and heat the plasma, which is consistent with the data. Regardless of the source of the instability, it seems to have the effect of quenching *K*-shell emission.

VI. CONCLUSION

The mathematical model and numerical methods that were widely used for the investigations of gas flows with phase transitions (spontaneous condensation) in power engineering and some other fields, have now been applied to the investigation of processes taking place in gas-cluster target formation. The applicability in principle of this model and this class of models has been shown for the investigation of spatial structure of gas-cluster targets. Good agreement was obtained between the hydrodynamics modeling and the experimental data. As a result, this modeling will facilitate nozzle design in order to create specific clustering conditions.

The analysis also revealed additional interesting information. The spectroscopy provides a detailed characterization of

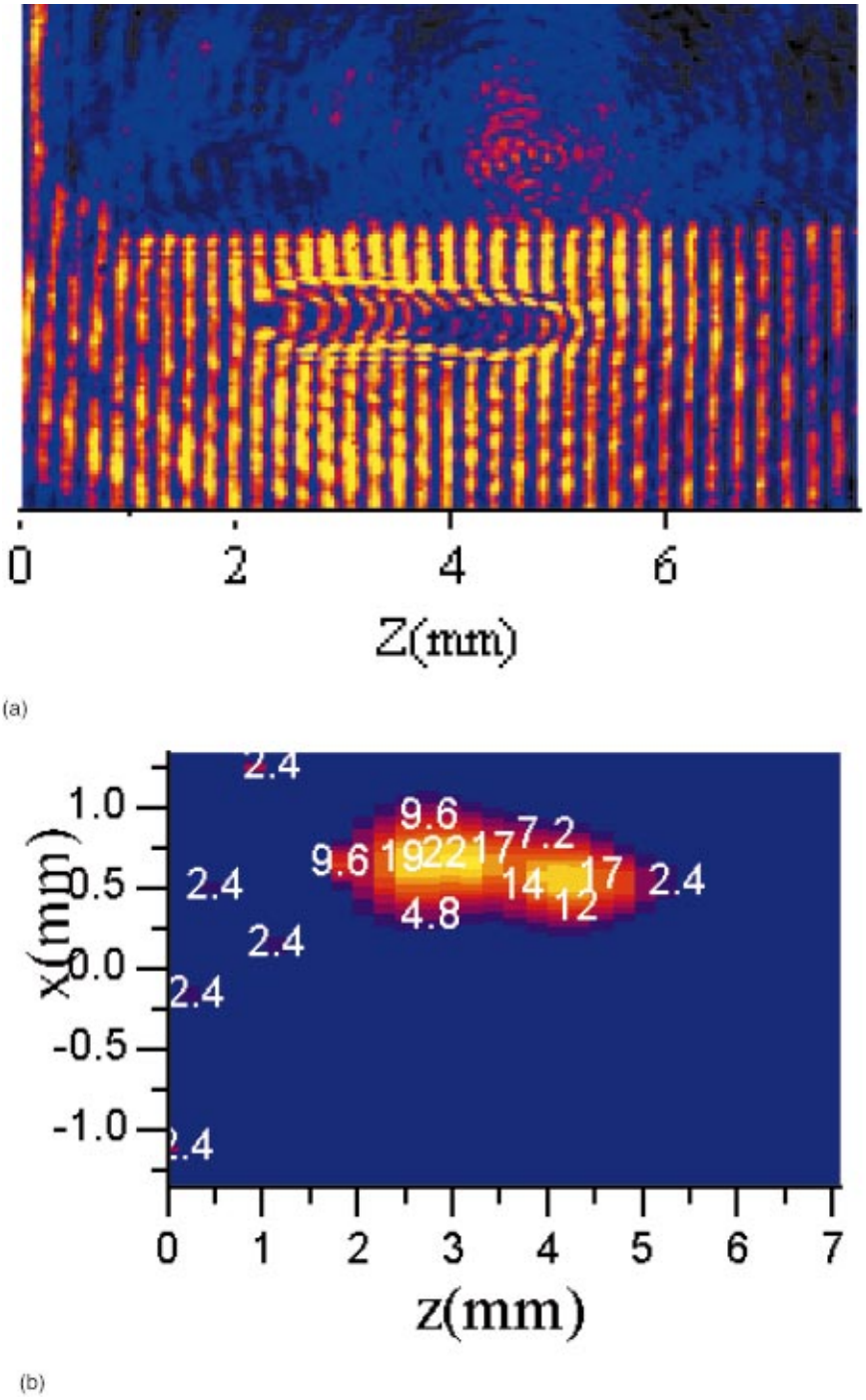

FIG. 9. (a) (Color) Interferogram is shown. The plasma density is fairly homogeneous for 3.5 mm along the direction of laser propagation. It appears to have only two small local maxima of the plasma density. Its length is close to the values of the jet diameter determined experimentally and theoretically with the current model (4 mm). (b) A false color plot of the electron densities determined from the interferogram. The maximum value that can be determined is about $N_e = 3 \times 10^{19}$ cm^{-3}. The downward displacement at $z = 3.5$ mm seems to come from the neutral density gradient toward the expansion direction that tends to deflect the beam from the nozzle.

the plasma, including its spatial structure. Spectroscopy is an excellent complement to interferometry by probing electron densities not accessible to interferometric techniques, and-vice versa. The spatial structure of the plasma is more dependent on laser and gas-jet parameters than the details of the large clusters employed in our experiments. Finally, the plasma over the first Rayleigh length is characterized by a relatively uniform temperature, density, and hot electron fraction, although laser intensity and resulting x-ray emission is strongly varying.

ACKNOWLEDGMENTS

This work was partly supported by the U.S. Department of Energy. A.Y.F. and T.A.P. appreciated the U.S. Civilian Research and Development Foundation (CRDF) Travel Grant Program for the possibility to present results of this article at several conferences.

[1] T. Ditmire, T. Donnelly, A. M. Rubenchik, R. W. Falcone, and M. D. Perry, Phys. Rev. A **53**, 3379 (1996).
[2] T. Ditmire, J. Zweiback, V. P. Yanovsky, T. E. Cowan, B. Hays, and K. B. Wharton, Nature (London) **398**, 6727 (1999).
[3] A. McPherson, B. D. Thompson, A. B. Borisov, K. Boyer, and C. K. Rhodes, Nature (London) **370**, 631 (1994).
[4] T. Ditmire, R. A. Smith, J. W. G. Tisch, and M. H. R. Hutchinson, Phys. Rev. Lett. **78**, 3121 (1997).
[5] Y. L. Shao, T. Ditmire, J. W. G. Tisch, E. Springate, J. P. Marangos, and M. H. R. Hutchinson, Phys. Rev. Lett. **77**, 3343 (1996).
[6] T. Ditmire, J. W. G. Tisch, E. Springate, M. B. Mason, N. Hay, R. A. Smith, J. P. Marangos, and M. H. R. Hutchinson, Nature (London) **386**, 54 (1997).
[7] T. Ditmire, J. W. G. Tisch, E. Springate, M. B. Mason, N. Hay, J. P. Marangos, and M. H. R. Hutchinson, Phys. Rev. Lett. **78**, 2732 (1997).
[8] E. M. Snyder, S. A. Buzza, and A. W. Castleman, Jr., Phys. Rev. Lett. **77**, 3347 (1996).
[9] S. Dobosz, M. Schmidt, M. Perdrix, P. Meynadier, O. Gobert, D. Normand, A. Ya. Faenov, A. I. Magunov, T. A. Pikuz, I. Yu. Skobelev, and N. E. Andreev, Pis'ma Zh. Eksp. Teor. Fiz. **68**, 454 (1998) [JETP Lett. **68**, 485 (1998)].
[10] S. Dobosz, M. Schmidt, M. Perdrix, P. Meynadier, O. Gobert, D. Normand, K. Ellert, T. Blenski, A. Ya. Faenov, A. I. Magunov, T. A. Pikuz, I. Yu. Skobelev, and N. E. Andreev, Zh. Eksp. Teor. Fiz. **115**, 2051 (1999) [JETP **88**, 1122 (1999)].
[11] J. Zweiback, R. A. Smith, T. E. Cowan, G. Hays, K. B. Wharton, V. P. Yanovsky, and T. Ditmire, Phys. Rev. Lett. **84**, 2634 (2000).
[12] E. Parra, E. Alexeev, J. Fan, K. Y. Kim, S. J. McNaught, and H. M. Milchberg, Phys. Rev. E **62**, 5931 (2000).
[13] P. Gibbon and E. Forster, Plasma Phys. Controlled Fusion **38**, 769 (1996).
[14] O. F. Hagena and W. Obert, J. Chem. Phys. **56**, 1793 (1972).
[15] O. F. Hagena, Surf. Sci. **106**, 101 (1981).
[16] O. F. Hagena, Rev. Sci. Instrum. **63**, 2374 (1992).
[17] B. M. Smirnov, Usp. Fiz. Nauk. **164**, 665 (1994) [Phys. Usp. **37**, 621 (1994)].
[18] A. B. Borisov, A. V. Borovskiy, V. V. Korobkin, A. M. Prokhorov, O. B. Shiryaev, X. M. Shi, T. S. Luk, A. McPherson, J. C. Solem, K. Boyer, and C. K. Rhodes, Phys. Rev. Lett. **68**, 2309 (1992).
[19] A. B. Borisov, A. McPherson, B. D. Thompson, K. Boyer, and C. K. Rhodes, J. Phys. B **28**, 2143 (1994).
[20] T. Ditmire, R. A. Smith, and M. H. R. Hutchinson, Opt. Lett. **23**, 322 (1998).
[21] G. S. Sarkisov, V. Yu. Bychenkov, V. N. Novikov, V. T. Tikhonchuk, A. Maksimchuk, S.-Y. Chen, R. Wagner, G. Mourou, and D. Umstadter, Phys. Rev. E **59**, 7042 (1999).
[22] T. M. Antonsen, Jr. and P. Mora, Phys. Rev. Lett. **69**, 2204 (1992).
[23] A. B. Borisov, A. McPherson, K. Boyer, and C. K. Rhodes, J. Phys. B **29**, L291 (1996).
[24] V. Malka, A. Modena, Z. Najmudin, A. E. Dangor, C. E. Clayton, K. A. Marsh, C. Joshi, C. Danson, D. Neely, and F. N. Walsh, Phys. Plasmas **4**, 1127 (1997).
[25] P. Mora and T. M. Antonsen, Jr., Phys. Plasmas **4**, 217 (1997).
[26] K. Ramachandran and V. K. Tripathi, IEEE Trans. Plasma Sci. **26**, 141 (1998).
[27] A. B. Borisov, S. Cameron, Y. Dai, J. Davis, T. Nelson, W. A. Schroeder, J. W. Longworth, K. Boyer, and C. K. Rhodes, J. Phys. B **32**, 3511 (1999).
[28] N. E. Andreev, M. V. Chegotov, M. C. Downer, E. W. Gaul, N. H. Matlis, A. A. Pogosova, and A. R. Rundquist, IEEE Trans. Plasma Sci., **28**, 1218 (2000).
[29] J. Fuchs, G. Malka, J. C. Adam, F. Amiranoff, S. D. Baton, N. Blanchot, A. Héron, G. Laval, J. L. Migel, P. Mora, H. Pépin, and C. Rousseaux, Phys. Rev. Lett. **80**, 1658 (1998).
[30] A. B. Borisov, A. McPherson, K. Boyer, and C. K. Rhodes, J. Phys. B **29**, L43 (1996).
[31] A. B. Borisov, A. McPherson, K. Boyer, and C. K. Rhodes, J. Phys. B **29**, L113 (1996).
[32] T. Auguste, P. D'Oliveira, S. Hulin, P. Monot, J. Abdallah, A. Ya. Faenov, I. Yu. Skobelev, A. I. Magunov, and T. A. Pikuz, Pis'ma Zh. Eksp. Teor. Fiz. **72**, 54 (2000) [JETP Lett. **72**, 38 (2000)].
[33] J. Abdallah, Jr., A. Ya. Faenov, T. A. Pikuz, M. D. Wilke, G. A. Kyrala, and R. E. H. Clark, J. Quant. Spectrosc. Radiat. Transf. **62**, 1 (1999).
[34] J. Abdallah, Jr., A. Ya. Faenov, I. Yu. Skobelev, A. I. Magunov, T. A. Pikuz, T. Auguste, P. D'Oliveira, S. Hulin, and P. Monot, Phys. Rev. A **63**, 032706 (2001).
[35] G. C. Junkel-Vives, J. Abdallah, Jr., F. Blasco, C. Stenz, F. Salin, A. Ya. Faenov, A. I. Magunov, T. A. Pikuz, I. Yu. Skobelev, T. Auguste, P. D'Oliveira, S. Hulin, P. Monot, and S. Dobosz, J. Quant. Spectrosc. Radiat. Transf. **71**, 417 (2001).
[36] I. Yu. Skobelev *et al.*, Zh. Eksp. Teor. Fiz. **108**, 1263 (1995) [JETP **81**, 692 (1995)].
[37] M. E. Deitch and G. A. Filippov, *Gas Dynamics of Two-Phase Media* (Energoizdat, Moscow, 1981).
[38] G. A. Saltanov, *Nonequilibrium and Nonstationary Processes in Gas Dynamics* (Nauka, Moscow, 1979).
[39] L. E. Sternin, *Principles of Gas Dynamics of Two-phase Flows in Nozzles* (Mashinostrojenije, Moscow, 1974).
[40] Ya. I. Frenkel, *Kinetic Theory of Liquids* (Nauka, Leningrad, 1981).
[41] A. S. Boldarev, V. A. Gasilov, F. Blasco, F. Dorchiez, C. Stenz, F. Salin, A. Ya. Faenov, T. A. Pikuz, A. I. Magunov, and I. Yu. Skobelev, in *Atomic Processes in Plasmas, Tenth Topical Conference*, edited by A.L. Osterheld and W.H. Goldstein, AIP Conf. Proc. No. 381 (AIP, Woodbury, NY, 1996).
[42] J. Abdallah, Jr., R. E. H. Clark, D. P. Kilcrease, G. Csanak, and C. J. Fontes, in *Space Technology and Applications International Forum*, edited by Mohamed F. Starace, AIP Conf. Proc. No. 361 (AIP, Woodbury, NY, 1996).